Angewandte Chemie
Eine Zeitschrift der Gesellschaft Deutscher Chemiker

Supporting Information

Bimetallic Ag-Pt Sub-nanometer Supported Clusters as Highly Efficient and Robust Oxidation Catalysts

Fabio R. Negreiros[+], Avik Halder[+], Chunrong Yin[+], Akansha Singh[+], Giovanni Barcaro[+], Luca Sementa, Eric C. Tyo, Michael J. Pellin, Stephan Bartling, Karl-Heinz Meiwes-Broer, Sönke Seifert, Prasenjit Sen, Sandeep Nigam, Chiranjib Majumder, Nobuyuki Fukui, Hisato Yasumatsu, Stefan Vajda, and Alessandro Fortunelli**

anie_201709784_sm_miscellaneous_information.pdf

Here we provide further size-selection and GISAXS data, Arrhenius plots for the COox reaction, and GIXANES data, fit of GIXANES spectra, and details on the computational approach, additional information on the energies of low-lying isomers and COox adsorption energies and reaction mechanisms for selected free and supported species.

Experimental Details

Figure S1. Mass spectrum of $Ag_NPt_M^+$ clusters.

Figure S2. Horizontal cuts of the two dimensional *in situ* GISAXS data collected on the Ag_9Pt_2 and Ag_9Pt_3 samples.

Figure S3. Horizontal cuts of the two dimensional *in situ* GISAXS data collected on the Ag_9Pt_2 and Ag_9Pt_3 samples – difference plots after subtraction of the blank and 25 °C data.

Figure S4. Arrhenius plot for the Ag_9Pt_2 and Ag_9Pt_3 samples.

Figure S5. XANES spectra of bulk Ag standards; *in situ* GIXANES spectra of Ag_9Pt_2 and Ag_9Pt_3 clusters collected at the silver and platinum edge.

Figure S6. Results from LCF analysis for alumina supported Ag_9Pt_2 cluster.

Figure S7. Results from LCF analysis for alumina supported Ag_9Pt_3 cluster.

Figure S8. Typical results of fits of GIXANES spectra by linear combination fitting (LCF).

Computational Approach

Figure S9. Five low-energy minima and their relative energies in eV with respect to the putative global minimum for Ag_9Pt_2 (left) and Ag_9Pt_3 (right). Ag atoms are in gray and Pt in red. Energies are in eV.

Figure S10. (a) Putative global minima of free Ag_9Pt_2 and Ag_9Pt_3. (b,c) Lowest-energy paths for CO oxidation on Ag_9Pt_2CO (b) and Ag_9Pt_3CO (c), respectively. Numbers represent adsorption energies of O_2/CO (the adsorption energy of the first CO molecule is 2.48 eV and the process is barrier-less) or energy variations due to internal structural changes, while values in square brackets represent reaction energy barriers. An Eley-Rideal mechanisms is identified by the ER symbol. Color coding for Ag and Pt as in **Figure S9**. Energies are in eV.

Figure S11. Structure and energetics of an O_2 molecule adsorbed at the interface between the metal cluster and the oxide surface on the bare Ag_9Pt_3 cluster and in presence of 1 or 2 adsorbed CO molecules. Structure and energetics of an O_2 molecule adsorbed on the Ag_9Pt_3 cluster in presence of 2 or three adsorbed CO molecules. Adsorption energies of CO are reported in black, while those of O2 are reported in red. Color coding for Ag and Pt as in **Figure S9**, while O and Al atoms in the substrate are in small dark red and blue spheres, respectively. Energies are in eV.

Figure S12. Atomistic depiction and energy diagrams for the lowest-energy COox path on (a) Ag_9Pt_2 and (b) Ag_9Pt_3 supported on the (0001) surface of α-alumina. Reaction energy barriers are indicated as "Bar" and are in eV. Color coding as in **Figure S11**. Energies are in eV.

Figure S13. Plots of the distribution of bond lengths for $Ag_9Pt_{2,3}$ species in the gas-phase and supported on the (0001) surface of α-alumina. Distances in Å.

References

Experimental Details

Support preparation. Amorphous alumina was used as support, because it resembles the catalyst supports widely used in industry and it has been proven excellent at immobilizing clusters [WinansTopCatal2006, VajdaNatMater2009]. In the present study a 3 monolayer thick (~0.7 nm) alumina film was prepared by atomic layer deposition (ALD) on top of the native oxide of a N-type (phosphorus doped) silicon wafer.

Sample preparation. The cluster samples were prepared in Cluster Research Laboratory of Toyota Technological Institute. The binary cluster ions were produced in a gas-aggregation chamber equipped with a dual magnetron-sputtering source with Ag and Pt targets. The details of the apparatus for the sample preparation have been reported elsewhere in detail [YasumatsuJPCS2009, YasumatsuEPJD2011]. In brief, the cluster ions having a desired atomic composition were selected using a quadrupole mass filter (Extrel MAX-16000). Next, the mass selected cluster ions passed through a collision cell filled with He gas at 100 K so as to reduce their kinetic energy and the diameter of the cluster beam, followed by soft landing of clusters in a circular area of 8 mm in diameter on the substrate with a kinetic energy of 1 eV per atom in a deposition chamber [YasumatsuRPP2003]. The number density of the Ag_9Pt_2 and Ag_9Pt_3 clusters on the support was set to 0.75 – 3.1 $\times 10^{12}$ cm^{-2}, in order to avoid agglomeration upon deposition. After deposition, the cluster samples were transported in air to Argonne National Laboratory for *in situ* characterization at the Advanced Photon Source. We note that during transport of the samples under air, the clusters may undergo oxidation.

Catalytic testing and in situ characterization. Temperature programmed reaction (TPRx) was used to measure the catalytic activity with a simultaneous collection of GISAXS and GIXANES data [LeeNIMPR2011]. Temperature programmed reaction (TPRx) was performed in fixed-bed, continuous flow reactor of own design [LeeNIMPR2011], under a 30 sccm flow of CO and O_2 (Air Gas) seeded in helium, at a $CO:O_2$:He=1:1:98 ratio, using calibrated mass flow controllers (Brooks model SLA5850). The pressure inside the reactor was kept above atmospheric pressure, at constant at 800 Torr by automated computer control. The cluster sample was placed on the top of a ceramic heater (Momentive Performance Materials Inc.) with a K-type thermocouple attached to its side. The applied temperature ramp is shown in **Figure 1**; it was programmed using a temperature controller (Lakeshore model 340), with a temperature deviation smaller than 0.5 ^oC. The sample was heated up to 300 ^oC in 50 ^oC steps with a slow heating rate of 10 ^oC/min, and the temperature was kept for 30 mins at each monitored temperature. To minimize the background and to get a flat baseline in the mass spectrometer for the monitored masses, the reactor was purged first with pure helium, followed by a continuous flow of the

reactant mixture for about 5 hours before the start of the temperature ramp. During TPRx, the formation of CO_2 was monitored using a differentially pumped mass spectrometer (Pfeiffer Vacuum Prisma Plus QMS 220), operated in multi-ion-detection mode (MID). To quantify the per cluster turn-over rate (TOR), the sensitivity of the mass spectrometer was calibrated by using certified gases (Air Gas). The TOR data reported in this paper are background corrected: The CO_2 signal detected over the blank alumina thin film (i.e. without the Ag-Pt clusters present) was subtracted from the CO_2 signal collected over the Ag-Pt sample. After background correction by subtracting the CO_2 signal collected under identical conditions on a blank (i.e. cluster-free) alumina support from the CO_2 signal acquired on the cluster sample , the CO_2 signal is converted into TOR based on the known metal loading / number of deposited clusters and calibration of the mass spectrometer with calibrated gases (Air Gas). The estimated uncertainty in the determined TOR value is around 5% or better. *In-situ* grazing incidence small angle X-ray scattering (GISAXS) and X-ray absorption near edge spectroscopy (GIXANES) in fluorescence mode detection mode was performed during the TPRx experiment. GISAXS with a geometry optimized for particles above 1nm was used to monitor possible sintering during the reaction. The GISAXS data were collected on a platinum detector (1024×1024 pixels) with X-rays of 25.5 keV as a function of temperature. The two-dimensional GISAXS images were then cut both in horizontal and vertical directions. The scattering is then compared with background on the alumina thin film and analyzed with Igor tool package Irena [IlavskyJAC2009]. GIXANES spectra were collected at the Pt L_3-edge and the Ag K-edge to follow the evolution of the oxidation state of Pt and Ag during CO oxidation, using a four-element Vortex detector mounted perpendicular to the beam (data collection at each absorption edge was performed using a pair of Ag_xPt_y cluster samples, i.e. a sample at the Pt L_3-edge and another sample at the Ag K-edge). The collected data were analyzed with IFEFFIT interactive software package (with ATHENA and ARTEMIS graphical interfaces). [Ravel2005] The GIXANES spectra for a wide range of bulk Pt and Ag bulk standards are collected to perform energy calibration and quantification of oxidization state of the Pt catalysts. For platinum Pt foil, $PtCl_2$ and PtO_2 as Pt^0, Pt^{II} and Pt^{IV} were used as standards, respectively. For silver Ag foil, Ag_2O and AgO were used for Ag^0, Ag^I, Ag^{II}, respectively. Activation energies are estimated from the temperature dependence of the TORs.

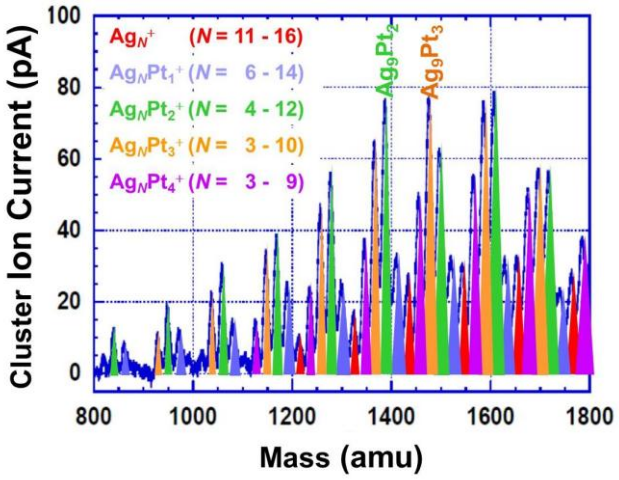

Figure S1. Mass spectrum of $Ag_NPt_M^+$ clusters produced in a dual-magnetron cluster-ion source, using 21 and 20 W DC discharge power on the Ag and Pt target, respectively, with the cluster ion flux measured on the deposition plate.

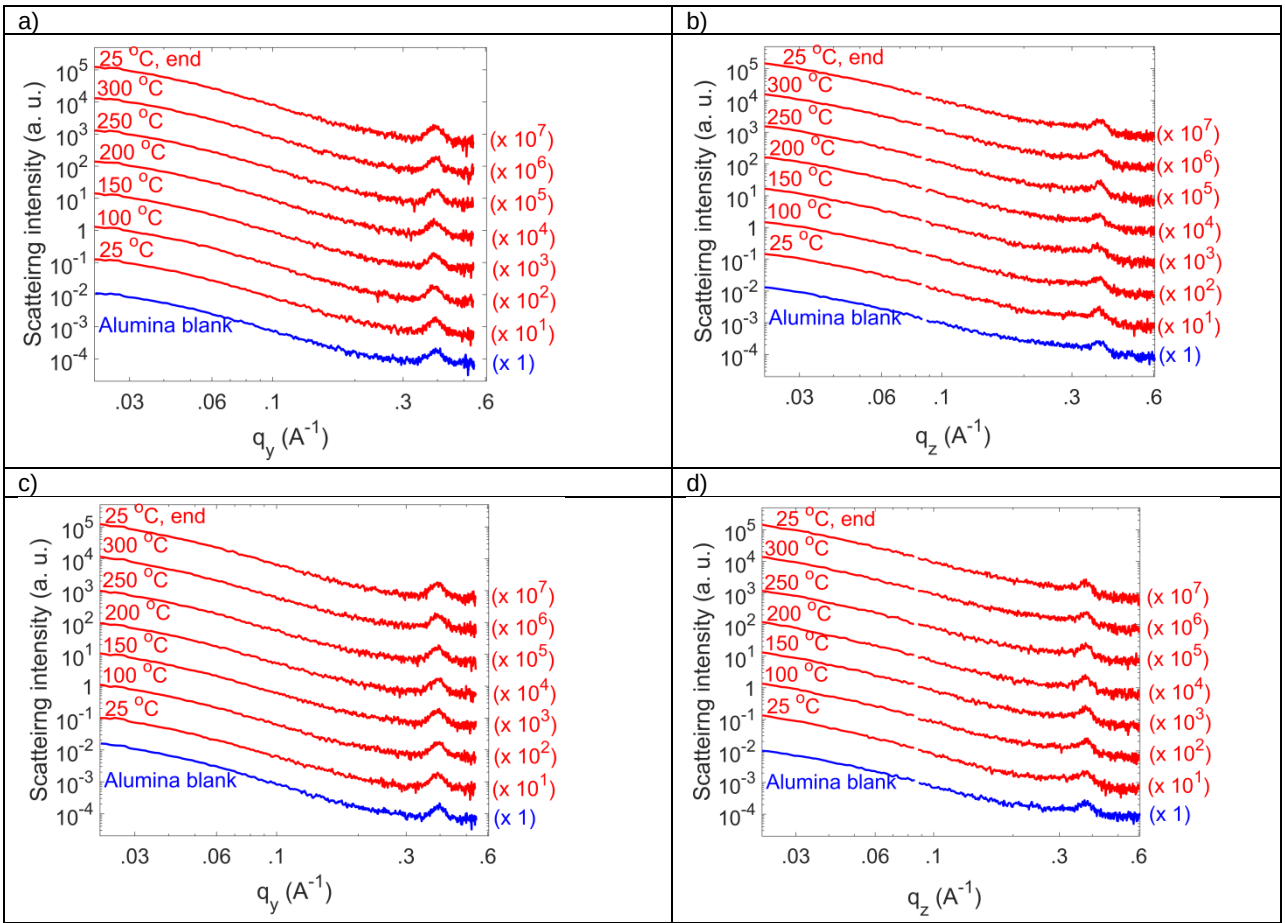

Figure S2. Horizontal (a) and vertical (b) cuts of the two dimensional GISAXS data collected *in situ* on the Ag_9Pt_2 cluster sample and alumina blank, averaged over 20 pixels of the 1024x1024 pixel Mar Gold detector used. Horizontal c) and vertical (d) cuts of the two dimensional GISAXS data collected *in situ* on the Ag_9Pt_3 cluster sample and alumina blank. The curves are rescaled by a factor marked at the right of individual curves for creating a relative offset. (The apparent bump at higher q of ~ 0.4 $Å^{-1}$ is an experimental artifact, a scattering by the Kapton window used to seal the *in situ* cell).There is no difference for the GISAXS pattern between the alumina blank sample and the cluster deposited alumina sample collected at any temperatures. The absence of any detectable SAXS signal is due to the weak scattering from 11 or 12 atom clusters as also reported by Dai et al for Pt_{12} clusters. [DaiJPCC2017]. The unaltered cuts taken at elevated temperatures also confirm that the clusters are sintering resistant Additional confirmation of sintering resistance of the bimetallic Ag-Pt clusters is based on the comparison with the GISAXS data obtained by Dai et al. [DaiJPCC2017] using a practically identical setup as used in our study, on monometallic Pt clusters of comparable size, where the smallest Pt cluster detected was Pt_{24} and was reflected through the appearance of a "bump" in the ~ 0.25 $Å^{-1}$ range, a pattern which is absent in the GISAXS data of the Ag_9Pt_2 and Ag_9Pt_3 clusters. Results of subtraction, from the cluster data, of the signal of the blank and the cluster signal at 25 °C are shown in **FigureS3**.

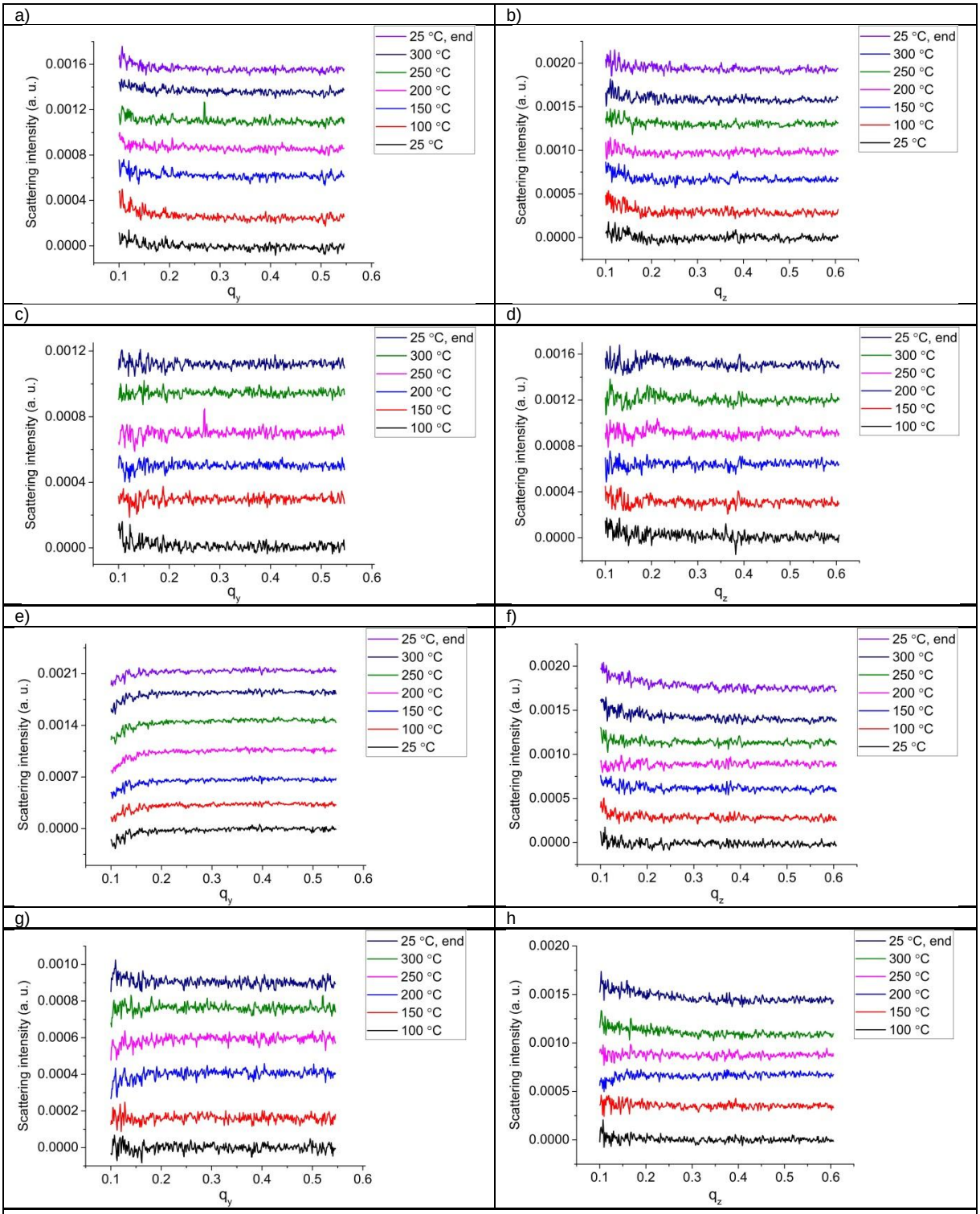

Figure S3. Horizontal (a) and vertical (b) cuts of the two dimensional GISAXS data collected *in situ* on the Ag_9Pt_2 cluster sample after subtracting the cut from the alumina blank. Horizontal (c) and vertical (d) cuts of the two dimensional GISAXS data collected *in situ* on the Ag_9Pt_2 cluster sample after subtracting the cut from the data at 25 °C. Horizontal (e) and vertical (f) cuts of the two dimensional GISAXS data collected *in situ* on the Ag_9Pt_3 cluster sample after subtracting the cut from the alumina blank. Horizontal (g) and vertical (h) cuts of the two dimensional GISAXS data collected *in situ* on the Ag_9Pt_3 cluster sample after subtracting the cut from the cluster data at 25 °C. All cuts were obtained by averaging over 20 pixels of the 1024x1024 pixel Mar Gold detector used for GISAXS data collection. The results from subtractions further confirm that a scattering

form the as deposited subnanometer clusters is not resolvable and that no sintering of clusters is taking place.

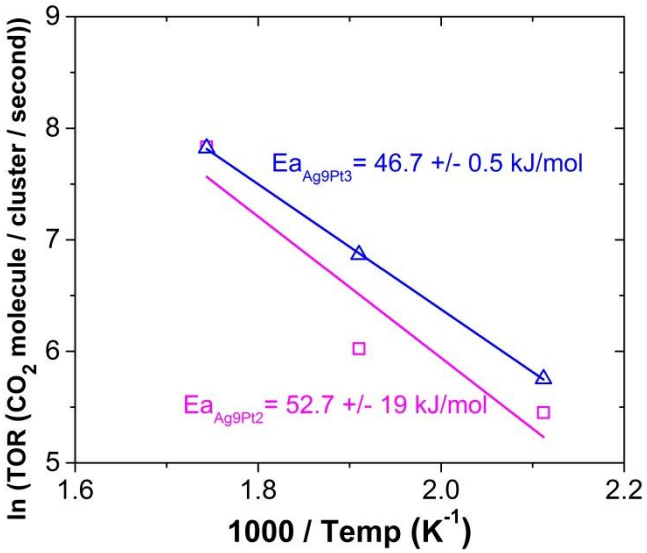

Figure S4. Arrhenius plot for Ag_9Pt_2 (pink) and Ag_9Pt_3 (blue) samples.

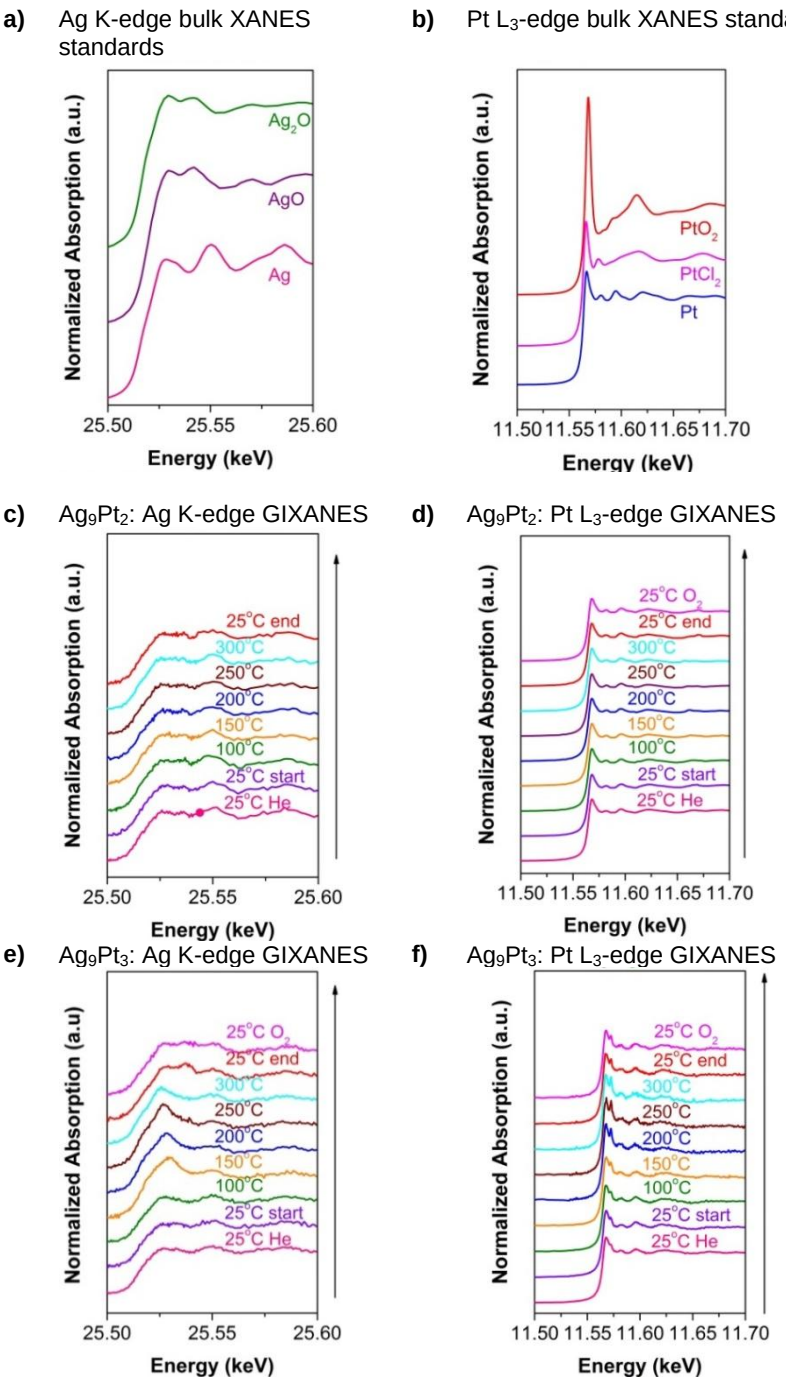

Figure S5. (a) XANES spectra of bulk Ag standards: Ag (Ag^0), Ag_2O (Ag^I), and AgO (Ag^{II}). (b) XANES spectra of bulk Pt standards: Pt (Pt^0), $PtCl_2$ (Pt^{II}) and PtO_2 (Pt^{IV}). *In situ* GIXANES spectra of Ag_9Pt_2 clusters collected at the silver K-edge (c) and platinum L_3-edge (d). *In situ* GIXANES spectra of Ag_9Pt_3 clusters collected at the silver K-edge (e) and platinum L_3-edge(f). See **Figure 1** for the applied temperature profile. Comparison of plots in (c) and (e) indicates higher oxidizability of Ag in the Ag_9Pt_3 cluster. We note the artefact – an apparent spike after the white line - in the 25 °C end spectrum at the Ag-edge in plot(e) and in the spectra at the Pt-edge in plot (f), coming from the detector. Those ~4-5 "bad" points were removed prior fitting of the spectra. The first data point labelled as (25 ˚C He) corresponds to GIXANES data collected under He at 25 ºC before the inlet of the CO and O_2 and the start of the temperature ramp. The last data point labelled as (25 ˚C, O_2) corresponds to XANES data collected under 1% of O_2 in He at 25 ºC after closing the flow of CO subsequent to the temperature ramp. This (25 ˚C, O_2) point was recorded to replicate conditions before the experiment, namely the transfer of samples under air between deposition and the *in situ* experiment.

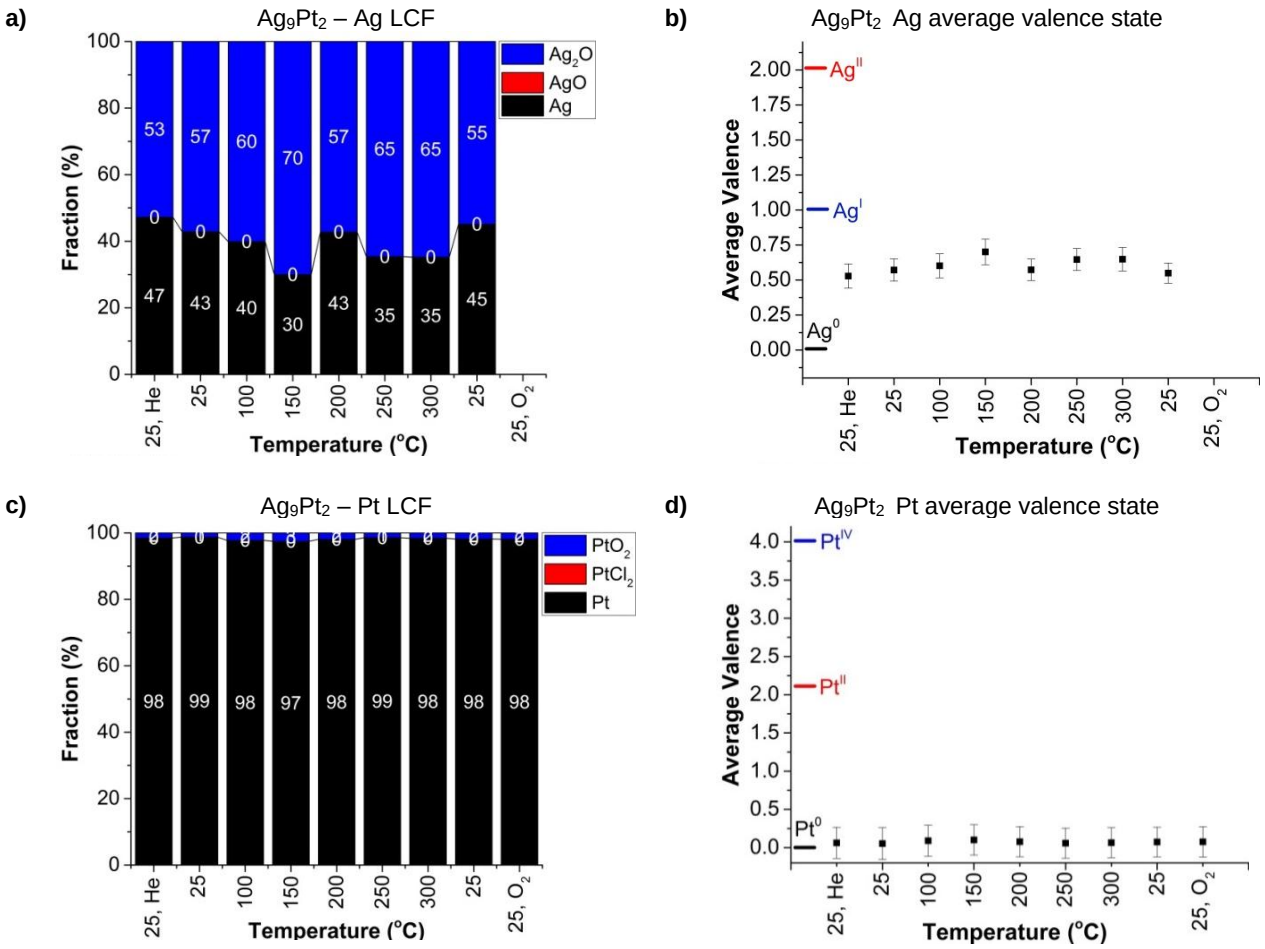

Figure S6. Results from LCF analysis of the *in situ* GIXANES spectra (**Figure S5c** and **S5d**) for the alumina supported Ag_9Pt_2 cluster. Left: The fraction of bulk components obtained from the fits of the GIXANES spectra. Right: Corresponding calculated average valence. The bulk XANES standards used in the analysis were as follows: Ag (Ag^0), Ag_2O (Ag^I), and AgO (Ag^{II}) for silver; and Pt (Pt^0), $PtCl_2$ (Pt^{II}) and PtO_2 (Pt^{IV}) for platinum (see **Figure S5a** and **S5b**). The first data point labelled as (25 ˚C, He) corresponds to XANES data collected under He at 25 ºC before the inlet of the CO and O_2 and the start of the temperature ramp. The last data point labelled as (25 ˚C, O_2) corresponds to GIXANES data collected under 1% of O_2 in He at 25 ºC after closing the flow of CO subsequent to the temperature ramp. This (25 ˚C, O_2) point was taken to replicate conditions before the experiment, namely the transfer of samples under air between deposition and the *in situ* experiment. Under the applied conditions, in Ag_9Pt_2/Al_2O_3 the average valence of both Pt and Ag is found to be rather stable at ~0 for Pt and ~0.6 for Ag. (Note that GIXANES spectra were not collected at the silver edge (25 ˚C, O_2).) The GIXANES spectra collected under helium at room temperature show clusters oxidized upon exposure to air, especially of their silver component. Typical LCF fit results are shown in **Figure S8**.

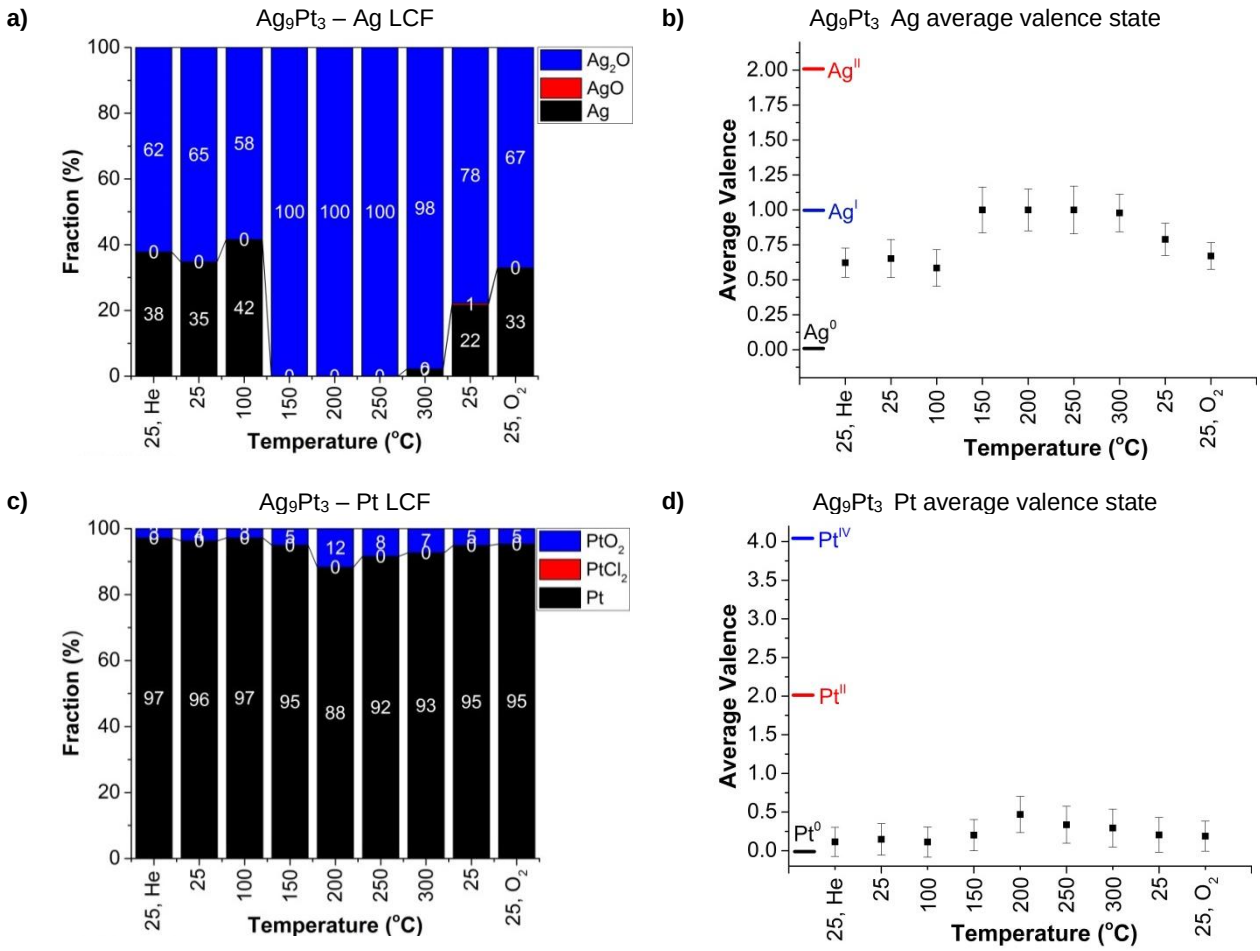

Figure S7. Results from LCF analysis of the *in situ* GIXANES spectra (**Figure S5e** and **S5f**) for the alumina supported Ag_9Pt_3 cluster. Left: The fraction of bulk components obtained from the fits of the GIXANES spectra. Right: Corresponding calculated average valence. The bulk XANES standards used in the analysis were as follows: Ag (Ag^0), Ag_2O (Ag^I), and AgO (Ag^{II}) for silver; and Pt (Pt^0), $PtCl_2$ (Pt^{II}) and PtO_2 (Pt^{IV}) for platinum (see **Figure S5a** and **S5b**). The first data point labelled as (25 ˚C, He) corresponds to XANES data collected under He at 25 ºC before the inlet of the CO and O_2 and the start of the temperature ramp. The last data point labelled as (25 ˚C, O_2) corresponds to XANES data collected under 1% of O_2 in He at 25 ºC after closing the flow of CO subsequent to the temperature ramp. This (25 ˚C, O_2) point was taken to replicate conditions before the experiment, namely the transfer of samples under air between deposition and the *in situ* experiment. The average valence of both Pt and Ag evolve coupled: both Pt and Ag start to get more oxidized at 150 ºC. At the highest applied temperatures Pt reaches a valence state of ~0.3-0.5 from ~0.1 at room temperature, while the valence state of Ag rises to ~1.0 from ~0.6. After cooled back to room temperature, the clusters regain their valence state as before the start of the temperature ramp. The GIXANES spectra collected under helium at room temperature show clusters oxidized upon exposure to air, especially of their silver component.

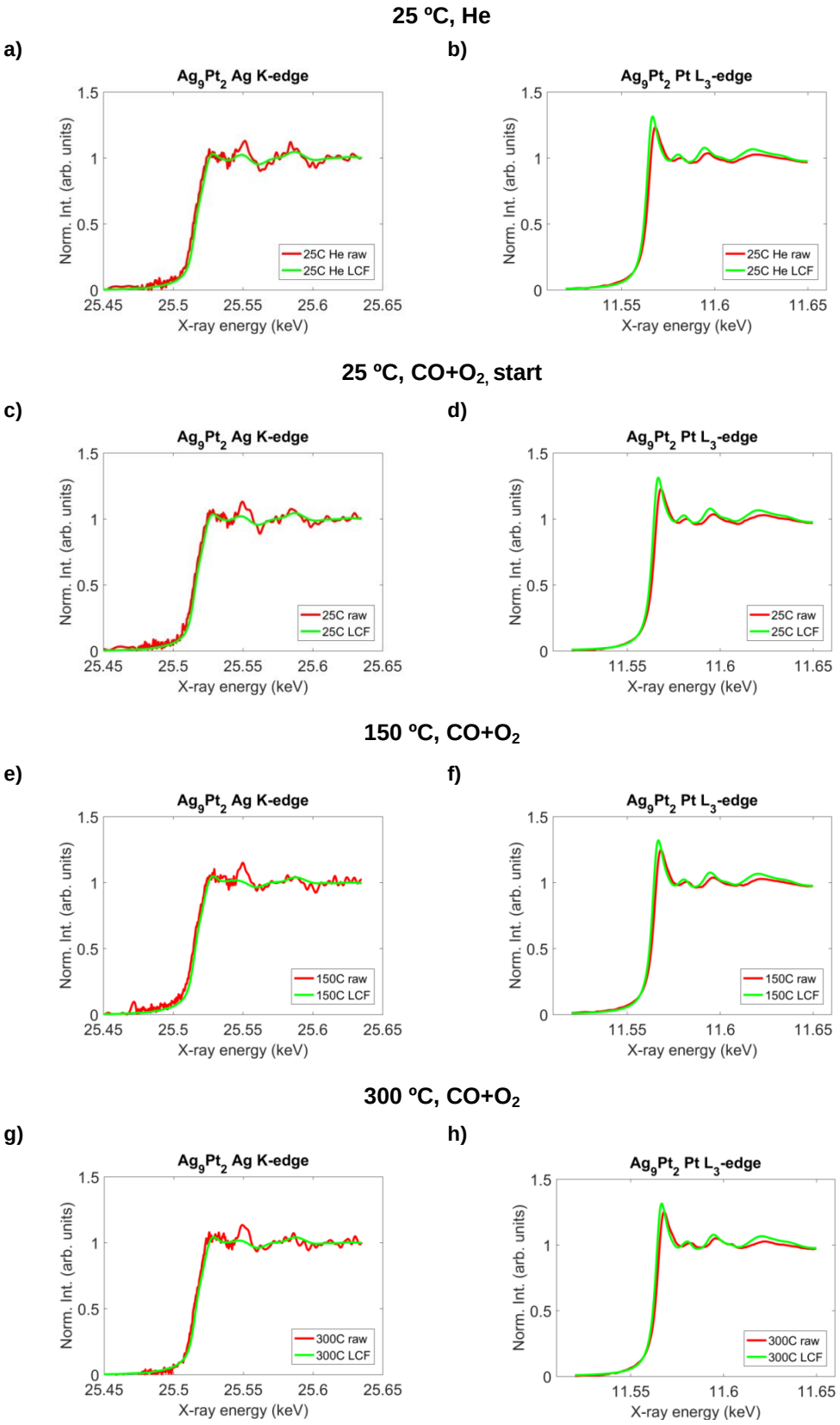

Figure S8. Typical results of fits of GIXANES spectra by linear combination fitting (LCF) with Ag (left) and Pt (right) bulk standards shown in **Figure S5a** and **S5b**, on the example of Ag_9Pt_2 cluster. Red: experimental data ("raw"), green: best fit ("LCF").

Computational Approach

For the DFT calculations on Ag-Pt clusters in the gas phase, the Quantum Espresso [GiannozziJPCM2009] plane-wave self-consistent field code (PWscf) is used, employing the Perdew-Burke-Ernzerhof (PBE) [PerdewPRL1996] exchange-correlation functional and ultra-soft pseudopotentials [VanderbiltPRB1990]. The following parameters are selected in the geometry optimizations: wave-function and charge-density cutoffs equal to 40 and 320 Ry, respectively, a face centered Bravais cubic cell with side length equal to 19 Å, a Gaussian smearing of 0.005 Ry, and a convergence threshold for self-consistency equal to 10^{-6} Ry. Geometry optimizations are performed spin unrestricted and using the Gamma-point for the integration in the reciprocal space. The geometries are considered to be converged when the forces on each atom become 0.01eV/Å or less.

For the DFT calculations on Ag-Pt clusters supported on an alumina surface, calculations are performed using both the Vienna ab initio Simulation Package (VASP) [KressePRB1996] (with an electron–ion interaction described by the full-potential all-electron projector augmented wave (PAW) method [BlochlPRB1994]) and the Quantum Espresso package with the same computational parameters employed for the gas-phase investigation. As in the gas phase, spin polarized calculations are performed using PBE exchange-correlation functional. The α-Al_2O_3(0001) surface is modeled with 7-atomic layer slab by truncating the bulk α-Al_2O_3 structure (a=b= 4.766 Å and c= 12.999 Å). It should be noted that in this model hydroxyl groups on the alumina surface are not considered. Experimentally, hydroxyls are found at ambient conditions, but their number gradually decreases as the temperature is raised until they finally disappear around ~500 °C [OttTSF1997]. Our model thus represents an alumina which, being fully dehydroxylated, realizes maximum adhesion of Pt clusters. Together with the results in the gas phase, this allows us to bracket the system's energetics and catalytic behavior. To avoid interactions between periodic slabs, we use a vacuum of about 10 Å between slabs. A large 3 x 3 super-cell (30 atom/per unit cell) is used to avoid interactions between images. Integration at the Gamma point only is used throughout all the calculations to reduce the computational effort, having verified that no significant quantitative difference exists with respect to a finer (2,2,1) grid. In the structural relaxation, only the 3 outermost layers of alumina are allowed to relax including a dipole correction [BengtssonPRB1999] to avoid any error due to interaction between adjacent images.

The search for the most stable structures for the Ag-Pt clusters in the gas phase is performed using a Basin-Hopping (BH) global search algorithm [LiPNAS1987] coupled with a DFT evaluation of energy and forces (i.e., a DF/BH algorithm) [ApraPRB2006, BarcaroCEJ2007]. We deploy a total of 1000 BH Monte-Carlo steps, random moves of 1.5 Å in the Cartesian directions of each atom, and a fictitious

temperature k_BT in the Monte-Carlo acceptance criterion of 0.4 eV. Once the most stable Ag-Pt structures are identified, the adsorption of one to few CO and/or O_2 molecules is investigated, considering the possibility of adsorbing more than one molecule on the same site. In addition, in the case of co-adsorption of CO and O_2, configurations corresponding to the formation of complexes containing CO_2/CO_3 species are also considered. Transition states are determined using the nudged elastic band (NEB) algorithm [HenkelmanJCP2000] using the Broyden scheme in a two-step approach: a first NEB on the full reaction path using 5-8 intermediate images and a somewhat lower accuracy (wave-function and charge density cutoffs in the range of 25/150 Ry to 35/280 Ry) in order to speed up this first path search, followed by a second NEB calculation with initial and final states close to the previously determined transition state, using 3 intermediate images and the climbing-image procedure to refine the value of the energy barrier and the transition state geometry.

Sampling of the potential energy surfaces (PES) of supported clusters is conducted in a less exhaustive way due to the cpu-demanding character of such simulations. Configurations selected from the most stable in the gas phase according to the previous investigation are positioned on the alumina surface, trying to explore as diverse an epitaxy as possible, and locally minimized. **Figure S13** compares the distribution of bond lengths for $Ag_9Pt_{2,3}$ species in the gas-phase and supported on the (0001) surface of α-alumina, showing that the clusters gets more compact after adsorption. On the lowest-energy configurations, the mechanism of CO oxidation is investigated by adsorbing CO molecules until saturation effects decrease the adsorption energies and then adsorbing O_2 molecules either on free sites or by replacing CO molecules, however again taking into account in the thermodynamic energy balance the loss of translational free energy of gas-phase O_2 and the difference between CO and O_2 adsorption energies in the case of replacement mechanisms. This is important because we expect that high-coverage effects are important to produce a ligand/cluster/support aggregate which is the real catalytically active species in heterogeneous ultrananocatalysis [NegreirosNS2012]. NEB calculations are performed using 5-8 intermediate images as in the gas phase.

In the calculations reported in **Figure S9-S12** a DFT/PBE approach is used. For the calculations reported in **Figure 3** of the main text, instead, dispersion corrections are introduced according to the Grimme-D2 model [GrimmeJCP2010]: as can be drawn from a comparison of the corresponding DFT/PBE and DFT/PBE-D2 energetics, dispersion terms selectively increase CO and O_2 adsorption energies. This increase is important to bring the prediction of kinetic modeling in better agreement with experiment.

To simulate COox reaction rates, a standard kinetic Monte Carlo (kMC) approach [GillespieJComputPhys1976] is used. The system is thus modeled as a graph whose nodes represents

cluster configurations, linked by and thus inter-converting via kinetic constants. In the case of Langmuir-Hinshelwood mechanisms, kinetic constants are calculated according to transition state theory [VineyardJPCSolids1957] and the Arrhenius equation in which energy barriers are taken from DFT/PBE-D2 calculations while Arrhenius prefactors are assumed to be equal to 10^{13} sec^{-1}. The kinetic constants of Eley-Rideal steps, in which a gas-phase molecule collides and reacts with a cluster/ligand complex giving rise to a modified complex – such as in the case of an O_2 molecule colliding with an adsorbed CO and giving rise to a CO_3 adsorbed species, are derived by: (i) calculating via DFT/NEB the transition state rate of the reverse (Langmuir-Hinshelwood) process, i.e., complex decomposition (e.g., $CO_3^{ads} \rightarrow CO^{ads} + O_2^{gas\text{-}phase}$), and thus calculating the corresponding kinetic constant via transition state theory as for a standard Langmuir-Hinshelwood step, (ii) invoking the microscopic reversibility principle to calculate the rate of the forward, Eley-Rideal process. Roto-vibrational contributions to free energies are neglected, while the translational contributions to free energy at a given temperature are included for gas-phase species. For example, the translational contribution to the free energy is assumed equal to 1.19 eV for CO and O_2 at 573 °K.

Atomic charges have been calculated according to the Bader approach [BaderBook1990]. For bare $Ag_9Pt_{2,3}$ clusters, in the gas phase the oxidation state of Ag ranges around 0.0/0.15 e for Ag_9Pt_2 and around 0.1/0.15 e for Ag_9Pt_3, while that of Pt is ≈0.35 e at both compositions. When adsorbed onto $\alpha(0001)$-Al_2O_3, the Ag atoms in contact with O ions of the support yield electrons to both the support and to the interface Pt and on average get significantly oxidized to 0.38 e, which is comparable to the average oxidation state of 0.5-0.6 e determined experimentally before COox reaction. Among the Pt atoms, after adsorption on the support the Pt at the surface gains only 0.03 e but the Pt at the interface gains a significant amount of electronic charge and its oxidation state becomes ≈0.7 e (this atom is close to a Al^{3+} cation which stabilizes this charge accumulation). It should be noted that the oxidation state of the Pt atom at the surface decreases after adsorption of a CO molecule and becomes basically neutral (≈0.07 e), and is consistent with experimental observations.

Finally, an interesting point concerns the adhesion energies of the clusters to the $\alpha(0001)$-Al_2O_3 support. For bare $Ag_9Pt_{2,3}$ clusters, the adhesion of Ag_9Pt_2 is 4.8 eV and that of Ag_9Pt_3 3.9 eV, which – among other phenomena connected with the 'metal-on-top' stabilization effect [BarcaroJCTC2005] – can be traced back to their different epitaxy to the support that brings 4 Ag atom in the former cluster and only 3 Ag atoms in the latter cluster in contact with O anions of the support (some other Ag atoms are in contact with Al^{3+} cations), with one additional Pt atom at the interface with the support in both cases. Neglecting the stronger adhesion of Pt due to electrostatic effects (see above), we can thus

estimate that each interfacial Ag atom contributes with ≈0.8 eV to the adhesion energy, while interfacial Pt contributes with at least ≈1 eV. These rough estimates are consistent with previous literature on pure Ag and Pt clusters [NigamLangmuir2010, NigamJPCC2012] and with the fact that the adhesion of single atoms is 1.9 eV for a single Ag, 2.5 eV for a single Pt, thus confirming that Pt is beneficial to stabilize and anchor the $Ag_9Pt_{2,3}$ clusters to the alumina substrate. It should be added that the distance between interfacial Pt and the closest Al^{3+} cation of the support is ≈2.5 Å, and is comparable with a typical Ag nearest-neighbor distance to O anion of the support of 2.2/2.6 Å (first-neighbor distances between interfacial Ag atoms and Al^{3+} cations range around ≈3 Å).

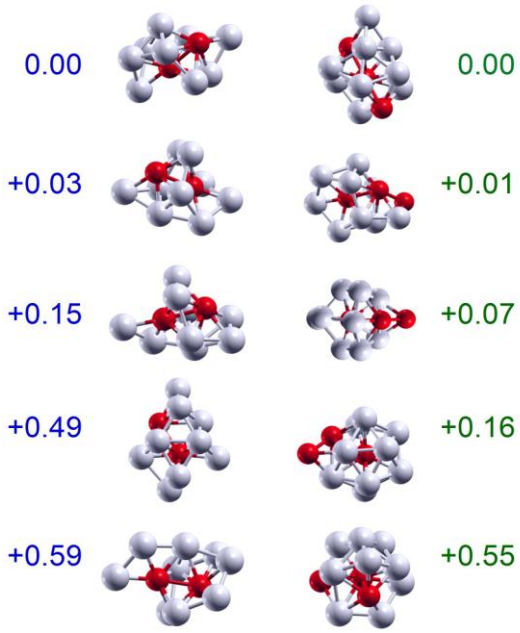

Figure S9. Five low-energy minima and their relative energies in eV with respect to the putative global minimum for Ag_9Pt_2 (left) and Ag_9Pt_3 (right). Ag atoms are in gray and Pt in red. Energies are in eV.

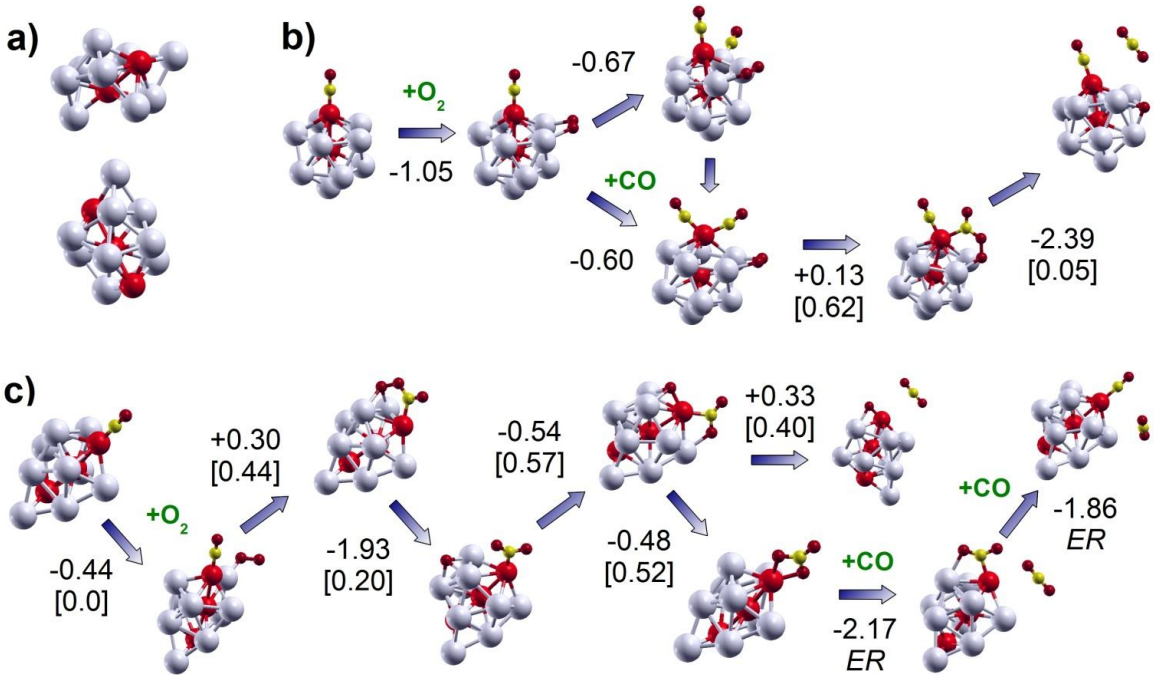

Figure S10. (a) Putative global minima of free Ag_9Pt_2 and Ag_9Pt_3 (additional minima are shown in **Figure S9**). (b,c) Lowest-energy paths for CO oxidation on Ag_9Pt_2CO (b) and Ag_9Pt_3CO (c), respectively. Numbers represent adsorption energies of O_2/CO (the adsorption energy of the first CO molecule is 2.48 eV and the process is barrier-less) or energy variations due to internal structural changes, while values in square brackets represent reaction energy barriers. An Eley-Rideal mechanisms is identified by the *ER* symbol. Color coding for Ag and Pt as in **Figure S9**. Energies are in eV.

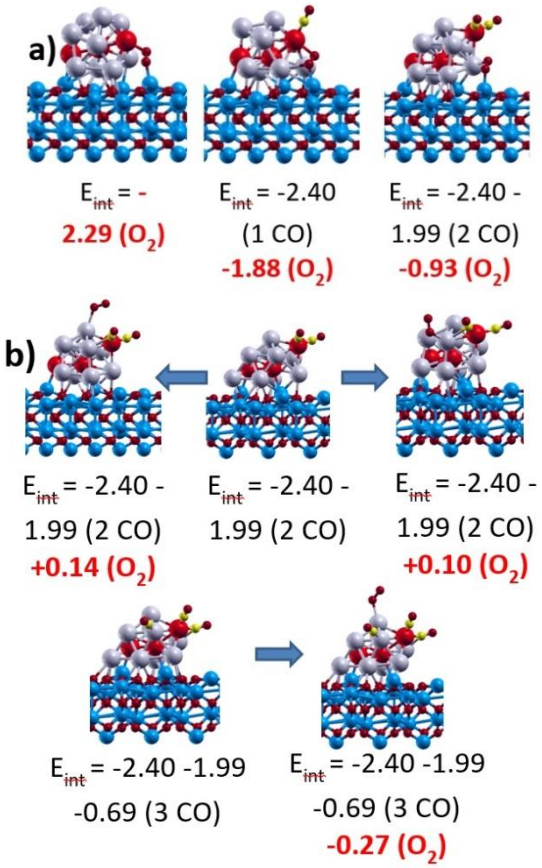

Figure S11. a) Structure and energetics of an O_2 molecule adsorbed at the interface between the metal cluster and the oxide surface on the bare Ag_9Pt_3 cluster (left panel) and in presence of 1 (central panel) or 2 (right panel) adsorbed CO molecules. b) Structure and energetics of an O_2 molecule adsorbed on the Ag_9Pt_3 cluster in presence of 2 (first row) or three (second row) adsorbed CO molecules. Adsorption energies of CO are reported in black, while those of O_2 are reported in red. Color coding for Ag and Pt as in **Figure S9**, while O and Al atoms in the substrate are in small dark red and blue spheres, respectively. Energies are in eV.

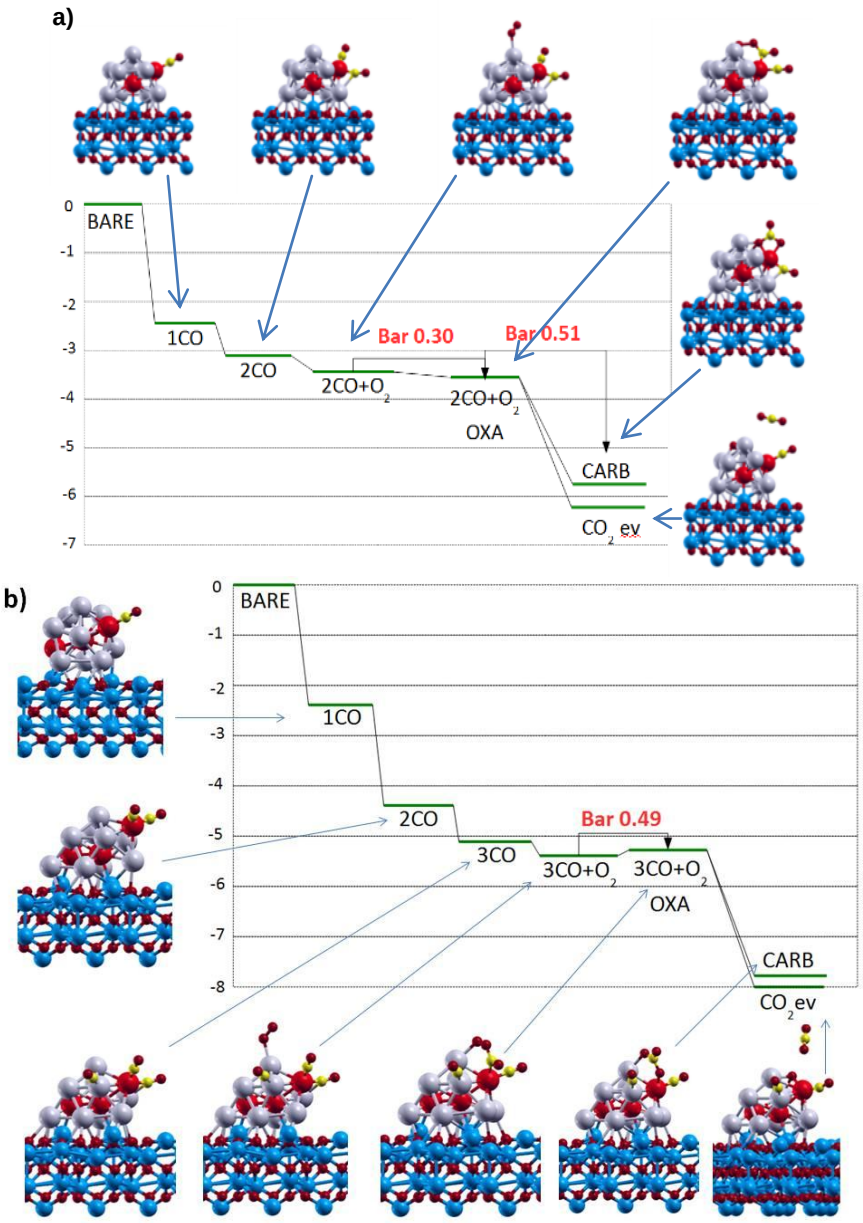

Figure S12. Atomistic depiction and energy diagrams for the lowest-energy COox path on (a) Ag_9Pt_2 and (b) Ag_9Pt_3 supported on the (0001) surface of α-alumina. Reaction energy barriers are indicated as "Bar" and are in eV. Color coding as in **Figure S11**. Energies are in eV.

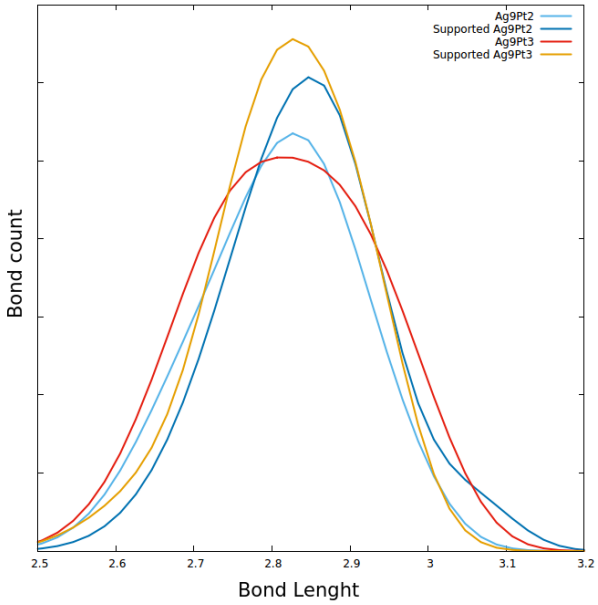

Figure S13. Plots of the distribution of bond lengths for $Ag_9Pt_{2,3}$ species in the gas-phase and supported on the (0001) surface of α-alumina. Distances in Å.

References

ApraPRB2006	E. Aprà, R. Ferrando, A. Fortunelli, Phys. Rev. B **2006**, *73*, 205414
BaderBook1990	R. F. W. Bader Atoms in Molecules: a Quantum Theory (New York, 1990, Oxford University Press).
BarcaroCEJ2007	G. Barcaro, E. Aprà, A. Fortunelli, Chem. Eur. J. **2007**, *13*, 6408-6418
BarcaroJCTC2005	G. Barcaro, A. Fortunelli, J. Chem. Theory Comput. J. **2005**, *1*, 972-985
BengtssonPRB1999	L. Bengtsson, Phys. Rev. B **1999**, *59*, 12301-12304
BlochlPRB1994	P. E. Blöchl, Phys. Rev. B **1990**, *50*, 17953-17979
DaiJPCC2017	Y. Dai, T. J. Gorey, S. L.Anderson, S. Lee, S. Lee, S. Seifert, R. E. Winans, J. Phys. Chem. C **2017,** *121*, 361-374
GiannozziJPCM2009	P. Giannozzi, et al., J. Phys. Condens. Mat. **2009**, *21*, 395502
GillespieJComputPhys1976	D. T. Gillespie, J. Comput. Phys. **1976**, *22*, 403-434
GrimmeJCP201	S. Grimme, J. Antony, S. Ehrlich, H. Krieg, J. Chem. Phys. **2010**, *132*, 154104
HenkelmanJCP2000	G. Henkelman, B.P. Uberuaga, H. Jónsson, J. Chem. Phys. **2000**, *113*, 9901-9904
IlavskyJAC2009	J. Ilavsky, P. R. Jemian, Irena: tool suite for modeling and analysis of small-angle scattering. Journal of Applied Crystallography **42**, 347-353 (2009)
KressePRB1996	G. Kresse, J. Furthmüller, Phys. Rev. B **1996**, *54*, 11169-11186
LeeNIMPR2011	S. Lee, B. Lee, S. Seifert, S. Vajda, R. E. Winans, Nuclear Instruments and Methods in Physics Research A **649**, 200-203 (2011)
LiPNAS1987	Z. Li, H.A. Scheraga, P. Natl. Acad. Sci. USA **1987**, *84*, 6611-6615
NegreirosNS2012	F.R. Negreiros, E. Aprà, G. Barcaro, L. Sementa, S. Vajda, A. Fortunelli, Nanoscale **2012**, *4*, 1208-1219
NigamJPCC2012	S. Nigam, C. Majumder, J. Phys. Chem. C **2012**, *116*, 2863-2871
NigamLangmuir2010	S. Nigam, C. Majumder, Langmuir **2010**, *26*, 18776-18787
OttTSF1997	A. Ott, J.W. Klaus, J.M. Johnson, S.M. George, Thin Solid Films **1997**, *292*, 135-144.
PerdewPRL1996	J.P. Perdew, K. Burke, M. Ernzerhof, Phys. Rev. Lett. **1996**, *77*, 3865-3868

Ravel2005	Ravel, B.; Newville, M., ATHENA, ARTEMIS, HEPHAESTUS: data analysis for X-ray absorption spectroscopy using IFEFFIT. *Journal of Synchrotron Radiation* **2005,** *12*, 537-541
VajdaNatMater2009	S. Vajda, M. J. Pellin, J. P. Greeley, C. L. Marshall, L. A. Curtiss, G. A. Ballentine, J. W. Elam, S. Catillon-Mucherie, P. C. Redfern, F. Mehmood, P. Zapol, Nat. Mater., 8, 213–216 (2009)
VanderbiltPRB1990	D. Vanderbilt, Phys.Rev. B **1990**, *41*, 7892-7895
VineyardJPCSolids1957	G. H. Vineyard, *J. Phys. Chem. Solids* **1957**, *3*, 121-127
WinansTopCatal2006	R.E. Winans, S. Vajda, G.E. Ballentine, J.W. Elam, B. Lee, M.J. Pellin, S. Seifert, G.Y. Tikhonov and N. A. Tomczyk *Top. Catal.* 39, 145-149 (2006).
YasumatsuEPJD2011	H. Yasumatsu, *Euro. Phys. J.* D, 63, 195-200 (2011)
YasumatsuJPCS2009	H. Yasumatsu, Masanori Fuyuki, Tetsuichiro Hayakawa and Tamotsu Kondow, *J. Phys. Conference Series*, **185**, 012057/1-4 (2009)
YasumatsuRPP2003	H. Yasumatsu, T. Kondow, *Reports on Progress in Physics*, **66**, 1783-1832 (2003)